Simultaneous Measurements and Modeling of the Electrochemical Impedance and the Cyclic Voltammetric Characteristics of Graphite Electrodes Doped with Lithium

M. D. Levi and D. Aurbach*

Department of Chemistry, Bar-Ilan University, Ramat-Gan 52900, Israel

Received: January 13, 1997; In Final Form: March 28, 1997[⊗]

Slow scan rate cyclic voltammetry (CV) and highly resolved (with respect to potential) electrochemical impedance spectroscopy (EIS) have been applied for lithiated graphite electrodes of different thicknesses. The impedance spectra have been successfully modeled for the whole range of intercalation potentials, using a combination of a Voigt-type equivalent circuit analog and the Frumkin and Melik-Gaykazyan (FMG) model. The Voigt-type analog, which is a series combination of $R||C$ circuits, models the Li ion migration through the surface films covering the graphite particles. The FMG model combines a finite-length Warburg element, which reflects solid state Li diffusion in the graphite particles in series with capacitance that reflects the bulk capacity of the graphite particles (doped with intercalated lithium). The highly anisotropic nature of the graphite particles predetermines different extensive properties, including their charge transfer resistance and the parameters of the finite-length Warburg. The application of small-amplitude EIS and slow scan rate CV to very thin graphite electrodes (micronic and submicronic thicknesses) enabled us to obtain a good separation of the various processes which take place along the intercalation reaction path (e.g., Li$^+$ migration through the passivating surface films, solid state diffusion of Li ion in graphite, electron migration across the boundaries of the graphite particles partly covered by the passivating films, interfacial charge transfer, accumulation−consumption of Li into graphite, and phase transition). The application of an electroanalytical model based on a Frumkin-type adsorption isotherm complicated with a slow charge transfer for the voltammetric behavior of these electrodes at slow scan rates is discussed.

Introduction

Since it was first reported that graphite is a good candidate as an anode material for application in lithium ion rocking chair batteries, the mechanism of intercalation of lithium ions into graphite has been the focus of intensive research.[1−7] The characterization of the lithium−graphite intercalation process has been mainly performed using galvanostatic charging, coupled, in some cases, with *in-situ* XRD (X-ray diffraction) technique.[1−3] Strong correlation between the results obtained by both techniques has created a reliable basis for identification of the lithium−graphite intercalation compounds. Comparison with other carbonaceous materials was helpful in understanding the unique nature of the phase transitions during lithium−graphite intercalation.[2]

The problem of the stability of graphite electrodes under cycling has attracted much attention in connection with the properties of the surface films formed on the surface of graphite particles when these electrodes are polarized to low potentials in Li salt solutions. Using FTIR (Fourier transform infrared) spectroscopy, a strong correlation between the surface chemistry of both lithium and carbonaceous materials has been observed.[8,9] Such a correlation results from the close proximity of an electrochemical window for the formation of lithium−graphite intercalation compounds to the standard potential of Li electrodes. However, the surface films are formed on graphite at potentials considerably more positive than the potential of the standard Li electrode.

The need for optimization of lithium ion batteries requires precise information on the mass and charge transport processes during the intercalation. In particular, solid state diffusion of lithium ions was studied by several transient techniques. Values

for chemical diffusion coefficients D, ranging from ca. 10^{-8} to 10^{-11} cm^2/s, were reported.[10−13] Different modes of electrode preparation, and thus different electrode porosity (and hence the cross-section for Li diffusion), make these D values calculated by different groups to be practically incomparable.

We have initiated a series of studies of the intercalation mechanism of Li in thin graphite-coated electrodes with the aim of better distinguishing between its different relaxation steps.[14−16] In this paper we report the results of simultaneous cyclic voltammetry (CV) and electrochemical impedance (EIS) characterization of the intercalation of lithium into graphite. The experimental data relate to three different electrode thicknesses. In order to reach high resolution, the scan rate (CV) was decreased to 4 μV/s, whereas the peak-to-peak alternative voltage in EIS was a few millivolts. The impedance spectra as a function of the type of the electrode and potential were appropriately modeled and compared with the corresponding CV characteristics, assuming one common intercalation mechanism. The mechanistic information on the phase transition processes obtained from the simultaneous EIS and CV measurements of these electrodes is also discussed.
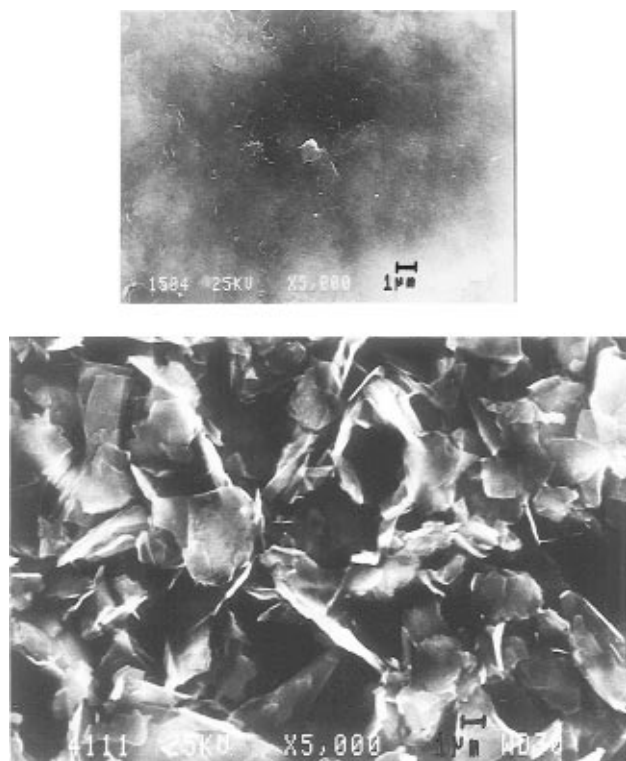
Experimental Section

Three graphite-coated electrodes of considerably different thicknesses, and probably compression, were prepared, using commercially available graphite powder KS-6 (Lonza). The graphite particles are flakes of average size, 6 μm, along the basal planes, which are about 0.1−0.5 μm thick. Ni or Cu foils were used as a metallic support. The active mass was comprised of 90% graphite and 10% PVDF (poly(vinylidenedifluoride)) as a binder.

The *thin* electrodes refer to a coating of about 10 μm thick, following the preparation procedure described elsewhere.[14] The *thick* electrodes were comprised of about 140 μm thick active

EIS and CV of Graphite Electrodes Doped with Li

J. Phys. Chem. B, Vol. 101, No. 23, 1997 **4631**

Figure 1. SEM micrographs of (a, top) of an ultrathin oriented graphite electrode and (b, bottom) a disoriented electrode.

graphite mass on a Cu grid support. The ultrathin electrodes were prepared as follows. A small amount of a mixture of powdered dry graphite and PVDF (9:1 by weight) was carefully rubbed onto the surface of a Ni foil (Goodfellow) 0.125 mm thick using fine filter paper. The rest of the powder was then removed with a fresh piece of filter paper. Using a micropipet, several drops of 1-methyl-2-pyrrolidone were added to the coating in order to achieve slight wetting before placing it in an oven. The coating was then repolished with filter paper.

The thin and the ultrathin electrodes were made of Ni or Cu foils (1.1 × 1.1 cm squares) covered on both sides with the active mass containing ca. 4 and 0.2 mg of graphite, respectively. The thick electrodes were approximately of the same mass as the thin ones (ca. 4 mg) but of lower size (4 × 4 mm).

A three-electrode cell was used for the electrochemical measurements in which a polyethylene frame with symmetrical slits on both sides holds the working and counter electrodes in a parallel plate configuration (Li counter and reference electrodes).

The electrolyte solution was 1 M $LiAsF_6$ (Lithco) in an ethylene carbonate (EC)−dimethylcarbonate (DMC) mixture (1:3) from Tomiyama (highly pure, Li battery grade). All of the other experimental details including exact cell configuration, solution preparation, instrumentation, glovebox operation, and the measurement performance were reported in previous publications.[14−21]

Results

a. Morphology of the Graphite Electrodes. All of the electrodes were examined by SEM. Figure 1a refers to a micrograph of an *ultrathin* electrode containing platelet particles oriented with their basal plane parallel to the substrate surface. For comparison, Figure 1b shows a micrograph of another *thin* coating of lower orientation. The surface of the oriented thin electrodes very much resembles that of the ultrathin electrode (Figure 1a). Using XRD technique, we usually observed a ca.

10-fold decrease in intensity of the characteristic 002 graphite peak for unoriented electrodes compared with the oriented ones (Figure 1a). Since the graphite particles are flakes of submicronic thickness which slide very easily and smoothly onto each other, careful electrode preparation provides a highly oriented electrode configuration in which the graphite platelets are compactly packed, forming a layered structure in which all of the basal planes of the flakes are horizontally oriented. Since the particles are irregularly shaped, there are enough pores (partly filled with the binder) to which the solution phase penetrates, and thus reaches most, if not all, of the active mass. Hence, we assume that all of the graphite flakes in the electrodes are in contact with the solution. Since the intercalation only takes place between basal planes, the cross-sectional area for the insertion of lithium into the graphite particles is the envelope of the four facets, perpendicular to the basal planes (about 4 × 6 × (0.1 → 0.5) μm^2 per particle; 3.3 and 0.15 cm^2 per geometric 1 cm^2 for the thin and ultrathin electrodes, respectively). It is clear from the above that the overall active cross-sectional area for the Li insertion process of an electrode is directly proportional to the amount of the active mass (graphite) in the electrode and thus to the electrodes' thickness (due to their high orientation). For all of the electrodes, the characteristic diffusion length should be taken as 3 μm, which is the average distance between the edges of the particles and their center.

The coating of the ultrathin electrode is apparently more dense than the thin one. Graphite is known to be a soft material, and thus, when rubbed and pressed onto the current collector, the platelets may be further split and may slide along each other without considerable change in the average size of the basal planes. Thereby, the preparation procedure of the ultrathin electrodes, by soft polishing, always provides compact coatings of submicronic thickness. Another point of importance is the fact that when intercalation potentials are reached, all of the graphite particles are already covered with surface films due to precipitation of the solvent and salt reduction products. These phenomena were fully described and discussed in previous publications.[8,9,16] In the present case, where the electrolyte system is EC−DMC−$LiAsF_6$, these surface films, which are also visible by SEM, are highly stable, protective, and passivating.

b. General Features of the CV and Z′,Z″−Nyquist Plots. Studying electrochemical intercalation of Li into graphite by LSV-CV, the most interesting and important picture is obtained at very low scan rates. From previous studies, it is known that by applying LSV to thin electrodes (prepared for the present study) at scan rates between 4 and 15 $\mu V/s$, we are beyond the control of the intercalation reaction by diffusion of Li in the bulk graphite, probing mostly the accumulation−consumption of Li into the graphite, as well as the reorganization and phase transition between intercalation stages. At these slow scan rates, the current was indeed found to be closely proportional to the potential scan rate (as expected for an adsorption type process). Figure 2 shows CV for all three electrodes at $\nu = 4$ $\mu V/s$. The charge involved in the processes of the thick and thin electrodes is the same. In order to compare them with the CV measured with the ultrathin electrode whose active mass was about 20−22 times smaller, the current measured from the ultrathin electrode was multiplied by a factor of 22; hence, the three CV could be presented in Figure 2 at the same scale, and the shape of the peaks could be compared. All three curves possess the same set of quasi-reversible peaks, marked as a, d, and e (major ones) and b and c (minor ones). As already reported and described, these peaks relate to charge transfer between different
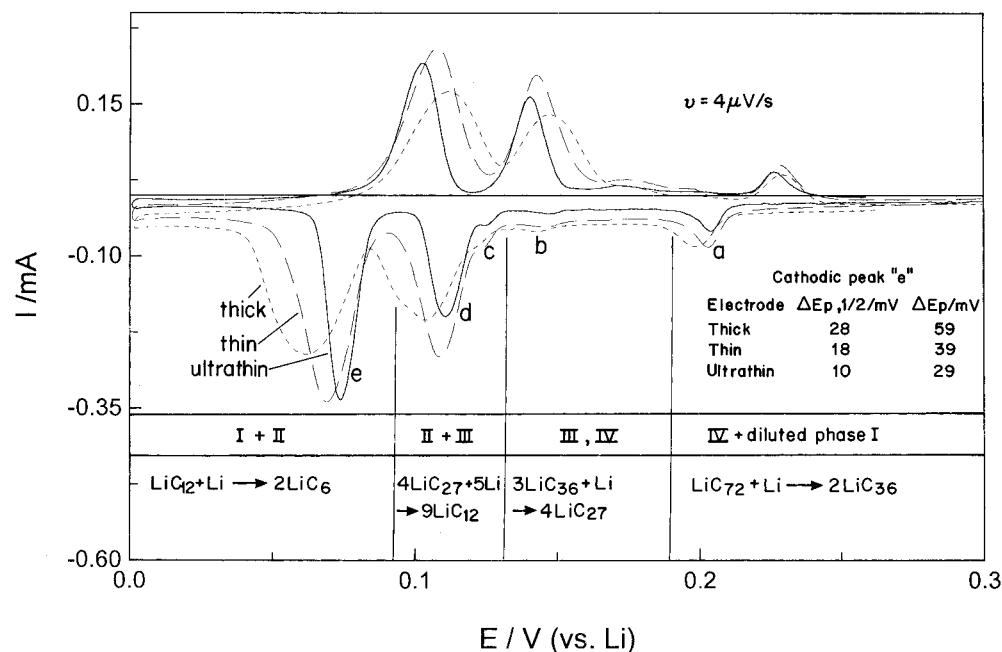
Figure 2. Slow scan rate cyclic voltammograms at $\nu = 4$ μV/s obtained with thick, thin, and ultrathin graphite coatings. Currents for the thick and ultrathin electrodes are normalized with respect to the thin one by multiplying their values by the ratio of the corresponding intercalation charge. Half-peak widths, $\Delta E_{p,1/2}$, and peak-potential separation, $-\Delta E_p$, the intercalation stages, and the phase transition reactions are indicated in the figure.
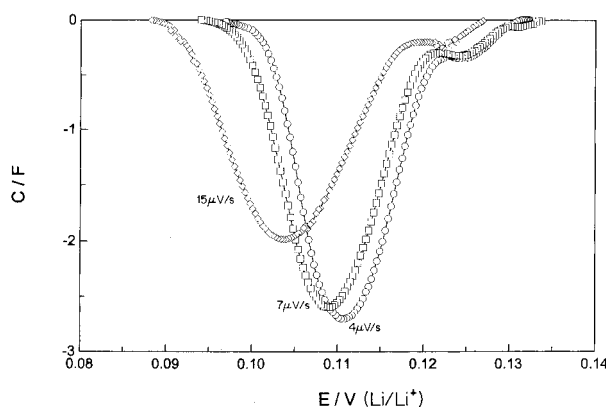
Figure 3. Normalized CV peak "d" (see Figure 2) for the ultrathin electrodes as a function of the potential scan rate. The current was divided by the scan rate, and thus the capacity is plotted *vs* the potential applied.

Li−C intercalation compounds. The relevant phases and attributed processes are also marked in Figure 2. In the series thick > thin > ultrathin, the peaks become narrower, with a corresponding decrease in the peak potential separation (the corresponding values are indicated in Figure 2). The considerable difference in peak widths may be attributed to different relaxation processes of the three electrodes accompanying the phase transitions. The resolution of the separation of the various electrode processes by applying different low scan rates depends not only on the coating thickness but also on the potential scan rate. The latter conclusion has been verified for the thin electrodes.[14] Figure 3 shows, as an example, the CV peak "d" for the ultrathin electrode normalized by the corresponding scan rate. From this figure it is seen that at the limit of a very low value of ν the CV peaks are characterized by a small and almost unchangeable value of the half-peak width (10 mV for $\nu = 4$ and 7 μV/s), with a slight shift of the peak potential toward more positive values. At higher potential scan rates ($\nu > 15$ μV/s), the current was proportional to the square root of the potential scan rate, this being typical of diffusion controlled processes.[14]

Identification of the nature of the rate-determining step for the curves in Figures 2 and 3 requires some modeling. Different mechanisms of coupling between *the accumulation−consumption* of Li into the graphite and secondary slow steps, such as diffusion, interfacial charge transfer, and migration of Li ions through the SEI (solid−electrolyte interface), can be relevant. The choice between them may be facilitated by parallel EIS measurements, since this technique is much more selective than CV with respect to the nature of the relaxation process involved.

Impedance spectra were measured from electrodes of the three different thicknesses. However, a comparison between the Nyquist plots obtained is not immediate due to the problem of their scaling factor, as the electrode's impedance depends directly on the cross-sectional area through which the electrochemical processes take place. However, as discussed in the previous section, the overall cross-section for the insertion of lithium into graphite in these electrodes is directly proportional to the total active mass per electrode unit area. The bulk capacity of the graphite, which influences the impedance spectra of the low frequencies and the interfacial capacitance and charge transfer resistance (including those related to Li$^+$ migration through the surface films) should be directly related to the electrodes' active mass since it determines the cross-sectional area for these processes. We conducted a series of experiments in which pairs of thin electrodes of different active mass were measured by both CV and EIS. When we multiplied the current values (CV) or the Z',Z'' values (EIS−Nyquist plots) obtained from these electrodes by the electrode's mass ratio, we could overlap both their voltammograms and the Nyquist plots obtained from them.

We thus conclude that, at least for a preliminary comparison of impedance spectra measured from electrodes of similar geometric area, but different active mass (and thus different thickness), the mass ratio of these electrodes could be used as a scaling factor.

With application of this scaling procedure, the characteristic Z'',Z'-plots for the ultrathin, thin, and thick electrodes are presented in Figure 4a,b for low and high intercalation levels, respectively. Qualitatively, all the spectra of Figure 4 have

EIS and CV of Graphite Electrodes Doped with Li

J. Phys. Chem. B, Vol. 101, No. 23, 1997 **4633**
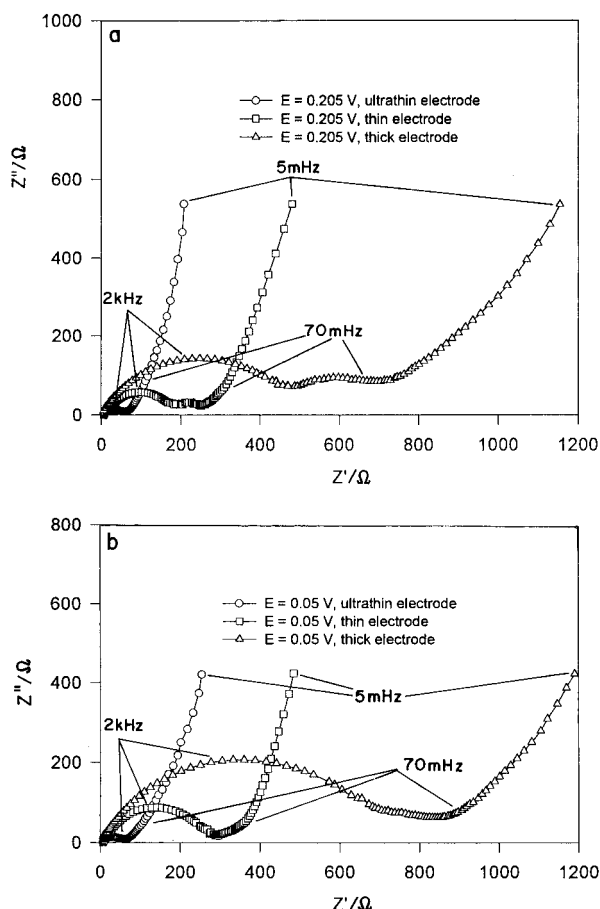
Figure 4. Nyquist plots for the thick, thin, and ultrathin graphite coatings (a) at the beginning of the intercalation and (b) in a fully intercalated state. The plots of the ultrathin electrode were normalized by multiplying the Z'' and Z' values by the ratio between the intercalation charge of the thin and thick electrodes (the same) and that of the ultrathin electrode.

similar features: a large flat semicircle related to the high-to-medium frequencies, a small semicircle related to the lower frequencies, and a sloping line of a changing slope, which becomes very steep at the lowest frequencies (the millihertz region). The distinction among these features in the spectra depends on the potential applied and the thickness of the active mass. Comparing this figure with Figure 2, one may notice that there is a correlation between both series of curves. Broadening of the CV peaks in the sequence ultrathin, thin, thick (Figure 2) corresponds well with a lesser slope of the Nyquist plots at low frequencies (Figure 4a,b).

c. Simple Model for CV and EIS of an Intercalation Process Complicated by Slow Charge Transfer. Modeling of very narrow CV peaks shifting with the scan rate (a shift which is not due to an ohmic IR drop) should reflect an intercalation process complicated by a slow interfacial charge transfer and thus can be based on an equation which combines the Frumkin intercalation isotherm with the Butler–Volmer equation for slow interfacial charge transfer, as already suggested:[14,22,23]

$$I = (k_0/\delta f\nu)\{(1 - X) \exp(-0.5gX) \exp[0.5f(E - E_0')] - X \exp(0.5gX) \exp[-0.5f(E - E_0')]\} \quad (1)$$

Here, I is the current taken for the convenience in a dimensionless form; k_0 is a standard heterogeneous rate constant for the charge transfer; E and E_0' are the electrode and the standard potentials of the redox couple, respectively; δ is the thickness

of the electrode coating; $f = F/RT$ with $F =$ Faraday constant, $R =$ gas constant, and $T =$ absolute temperature; g is the interaction constant from the Frumkin isotherm (negative for attraction interactions and positive for a repulsion); and X is the intercalation level (which depends on the electrode potential according to the Frumkin isotherm).

At equilibrium (high k_0, low δ and ν), the net current is zero. Thus, eq 1 is reduced to the Frumkin type isotherm:

$$X/(1 - X) = \exp[f(E - E_0')] \exp(-gX) \quad (2)$$

Note that the standard potential E_0' corresponds to the *equilibrium peak potential* (at which $X = 0.5$) only for the Langmuirian intercalation isotherm (i.e., at $g = 0$). Strong attraction between the intercalation sites obviously results in its shift toward lower potential values (25.7 mV for $g = -2$, 51.4 mV for $g = -4$, etc.). In this work it was indeed necessary to redefine the E_0' values for the Frumkinian condition (i.e., attractive interaction $g \neq 0$) accordingly, thus taking these shifts into account. The exchange current can be derived from either of the two terms in eq 1 (using the appropriate E_0' values). Raising both sides of eq 2 to the -0.5 power and substituting the correspondent term in the expression for the cathodic current yield the dimensionless exchange current I_0^{dim}:

$$I_0^{dim} = (k_0/\delta f\nu)X^{0.5}(1 - X)^{0.5} \quad (3)$$

Equation 3 can be rewritten for the conventional current dimension:

$$I_0 = Q_t k_0 X^{0.5}(1 - X)^{0.5}/\delta \quad (4)$$

where Q_t is the total intercalation charge relevant to the specific CV peak explored.

Thus, the charge transfer resistance R_{ct} is of the following form:

$$R_{ct} = \delta/fQ_t k_0 X^{0.5}(1 - X)^{0.5} \quad (5)$$

Equation 4 is comparable with the classical expression for the interfacial charge transfer limitation (without coupling with the accumulation–consumption step).[24]

The classical expression, though showing similar power dependence of X, deals with the independent concentrations of oxidant and reductant (redox) in solution phase, whereas eqs 4 and 5 deal with mole fractions X of the intercalated species. It should be noted that the product $X(E)(1 - X(E))$ has a maximum near the peak potential. Consequently, R_{ct} in eq 5 has a minimum at the peak potential.

Equations 1 and 5 can be used for direct comparison between theoretical and experimental CVs and Z'',Z'-plots. As an example of the application of eq 1 for simulation of CV curves, Figure 5 compares the theoretical curve with the experimental data for a thin electrode at $\nu = 4$ μV/s around peak e (phase II → phase I transition; see Figure 2). The fitting procedure of theoretical CV curves to experimental ones based on eq 1 has already been described.[14] In brief, this equation has two parameters, k_0 and g, which are characteristic of the specific intercalation process (which appears as a CV peak). Since we may obtain several CV curves at different and slow enough scan rates (ranging from 4 to 15 μV) to which eq 1 is applicable, we have enough data for iteration using a homemade program based on the Quatro Pro software.[14] As demonstrated in Figure 5, excellent agreement was obtained between the theoretical and the experimental curves related to peak e, using the following values of parameters $g = -4$ and $k_0 = 4.2 \times 10^{-7}$ cm/s.
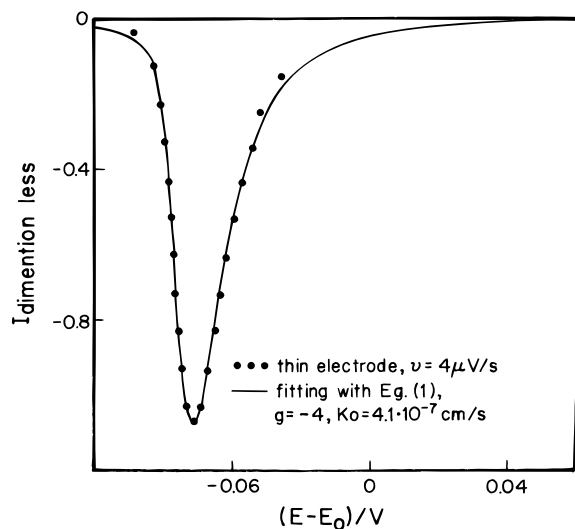
Figure 5. Comparison between the experimental CV curve for the thin electrode peak "e" ($\nu = 4\mu$V/s) and its theoretical fitted curve based on eq 1.
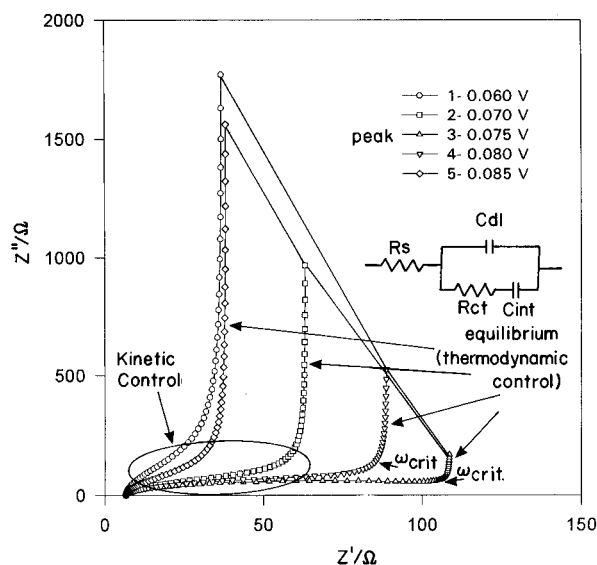
Figure 6. Theoretical Nyquist plots calculated according to the equivalent circuit analog shown in the figure at different potentials. The points on the curves at $\omega/2\pi = 5$ mHz were connected by a solid line and have a peak shape, with a minima at a potential close to the CV peak potential. The domains related to kinetic and thermodynamic control are marked.

It should be noted that all of the peaks obtained with the thin electrodes at slow enough scan rates (4–15 μV/s) could be simulated by eq 1 (as has already been demonstrated).[14] In contrast, the peaks in the CV measured from ultrathin electrodes, which are narrower (at the same scan rates) compared with those measured with the thin electrodes, could not be fitted so nicely to $I(E)$ curves calculated by eq 1. Hence, the electroanalytical response of these electrodes depends on their morphology. Reasonable conclusions on possible coupling between intercalation and charge transfer steps (which depend on the electrode's structure) can be drawn by a simultaneous application of EIS.

The simplest equivalent circuit analog that can be fitted for simulating impedance spectra of intercalation processes, and which is in line with the above model used to simulate the CV curves, is presented in Figure 6. The circuit includes solution resistance (R_s) in series with a Randles-type circuit, in which C_{dl} is parallel to the charge transfer resistance (R_{ct}) connected with the intercalation capacitance (C_{int}) which simulates the

accumulation–consumption step of lithium into the bulk graphite. A similar circuit has been proposed for simulating adsorption of a species on electrodes.[25a,26a] R_s and C_{dl} were extracted directly from the experimental data. The connection between EIS and CV models is expressed by the formula $C_{int}(E) = I_{CV}/\nu$ (which is commonly used for treatment of adsorption on interfaces), where I_{CV} is the CV current. R_{ct} depends on E according to eq 5 *via* the intercalation isotherm $X = X(E)$.

It should be emphasized that we do not expect that this simple model is sufficient to describe the highly complicated case of the lithium–graphite intercalation process. However, it is important to analyze this simple model as an introduction to the more rigorous modeling presented in the next section because this simple model shows how data from slow scan rate CV and EIS can be correlated and what the key features and parameters are on which to concentrate in such a correlation.

Figure 6 also shows theoretical Nyquist plots at potentials close to the CV peak e, based on the above simplified model. Parts a–d of Figure 7 present a typical family of Nyquist plots obtained with the ultrathin electrode at different intercalation levels X. They are divided into three groups (a–c), corresponding to potential domains around the three major peaks observed in the CV curves, a, b, and e (respectively). Figure 7d shows in an enlarged scale the high-frequency domain of these plots.

Comparison between Figures 6 and 7c (the same potential domain) shows some important common features between the theoretical and the experimental curves. In both sets of curves, a *peak-shaped* dependence of the imaginary part of the impedance on E at the lowest frequency measured $\omega/2\pi = 5$ mHz is observed. At the lowest frequencies, the impedance spectra measured from these electrodes reflect capacitive behavior due to the bulk intercalation capacity of the graphite. Hence, a minimum in Z'' means a maximum in C_{int}. The minimum in Z'' at 5 mHz appears in both the experimental and the theoretical series around the peak potential which correlates nicely with the expected maximum in the electrode capacity at the CV peak. Another point of interest which is demonstrated by the simplified model of Figure 6 is the separation between the kinetic (high-medium frequencies) and the thermodynamic control (low frequencies). It is possible to define $\omega_{critical}$ in which the impedance spectra reflect the change from kinetic to thermodynamic control (as marked in Figure 6). This $\omega_{critical}$ corresponds to a critical potential scan rate below which the cyclic voltammograms reflect the accumulation–consumption adsorption-type behavior, and above it they also reflect diffusion processes. The impedance spectra of Figure 7 also reflect such a separation. However, both the low-frequency domain for the thin electrodes, in which the slope of Z'' *vs* Z' is not vertical, and the fact that such a good fitting was found between the CV and the model based on eq 1 reflect a situation in which even when the behavior of these electrodes is basically thermodynamically controlled, there is some involvement of slow kinetics. This, for instance, may be due to problems of electrical contact between the carbon particles in the composite electrode and/or some (minor) continuous reduction of solution species through defects in the surface films. As expected, the agreement between both series of curves (Figures 6 and 7) is completely unsatisfactory in the *medium- to high-frequency domain* because of two major processes which are not taken into account in this model: solid state diffusion of lithium ions and the *migration* of Li ions through the surface films which cover the graphite. A model which takes these processes into account is discussed below.

EIS and CV of Graphite Electrodes Doped with Li

J. Phys. Chem. B, Vol. 101, No. 23, 1997 **4635**
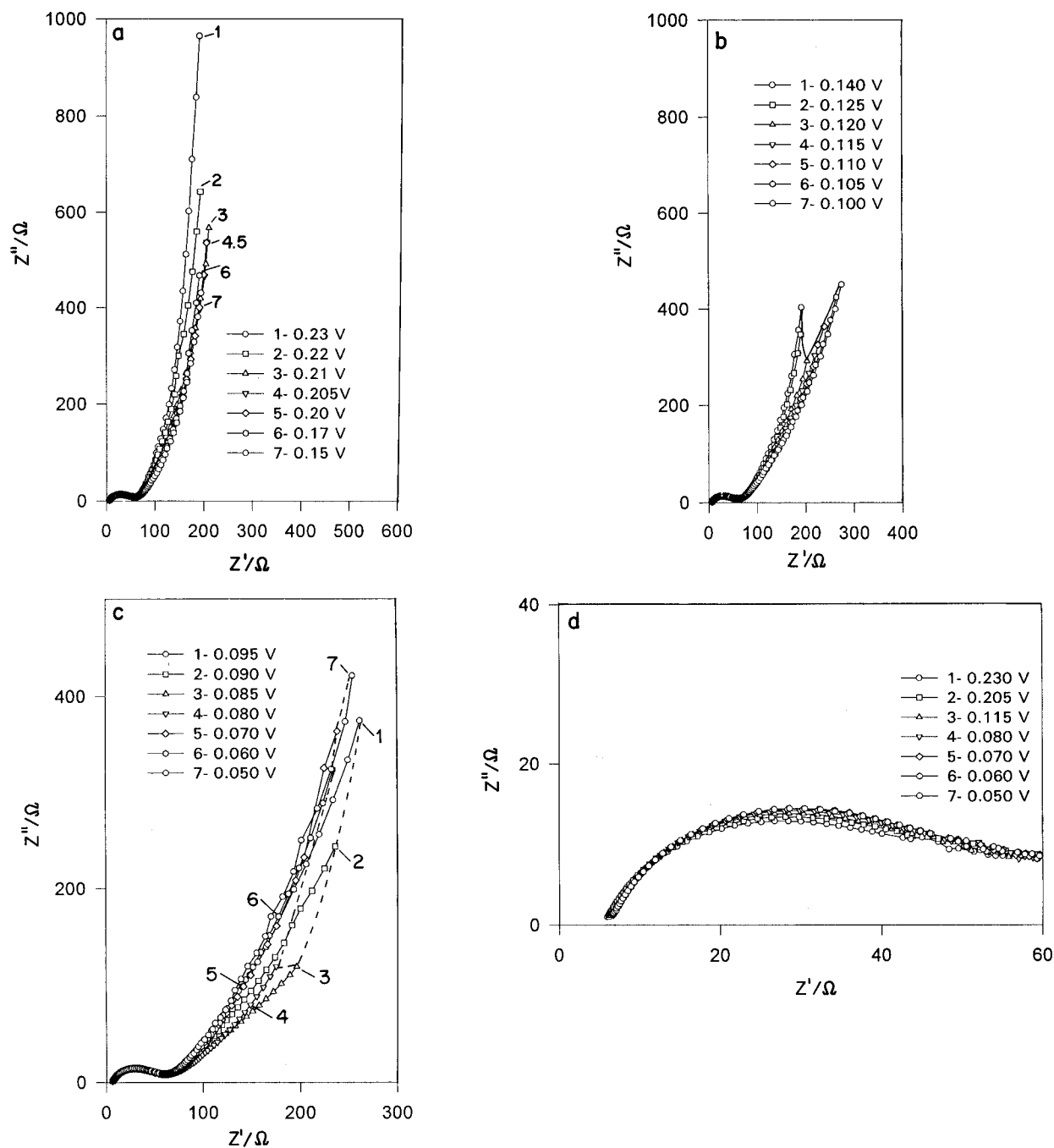
Figure 7. Experimental Nyquist plots for the ultrathin electrode measured at different potentials in the vicinity of the CV peaks "1", "4", and "5" in a–c, respectively. In d, the high-frequency domain is shown in an expanded scale. The points on the curves at the lowest frequency, 5 mHz, were connected with a solid line in (b) and with a dashed line in (c) (which shows a peaklike shape).

d. Generalized Frumkin and Melik-Gaykazyan (FMG) Impedance Model. Modeling impedance spectra by equivalent circuit analogs always raises the problem of ambiguity. It is well-known that the same complicated impedance spectrum may be fitted very nicely by several different equivalent analogs. However, when the physicochemical situation of the electrochemical systems are clear and the choice of the model is based on parallel morphological spectroscopic, and electroanalytical studies, then it may considerably reduce the ambiguity and enable a preferred circuit analog to be decided on. In the case of the lithium–graphite intercalation process, it is clear that there are several processes which occur in series: ion conduction in solution, diffusion of ions in solution to the interface, migration of Li ions through the surface films, charge transfer, solid state

diffusion, and finally, accumulation, which is a capacitive-type behavior. Hence, an equivalent circuit analog suitable for describing these processes should include elements in series. It therefore seems that the development of the model as described below is straightforward, and in fact the physicochemistry of the systems studied naturally channels the simulation of the impedance spectra obtained toward such a model.

This model in its particular form was first introduced to describe adsorption of organic molecules on a mercury electrode.[27] The corresponding equivalent circuit consisted of a double-layer capacitance C_{dl} in parallel with a combination of a Warburg-type element and a resistance (in series) due to the slow adsorption process itself.[26b,27] We modified this equivalent analog by substituting the infinite-length Warburg $Z_{w\infty}$ element with its finite-length analog Z_w due to the finite-diffusion length
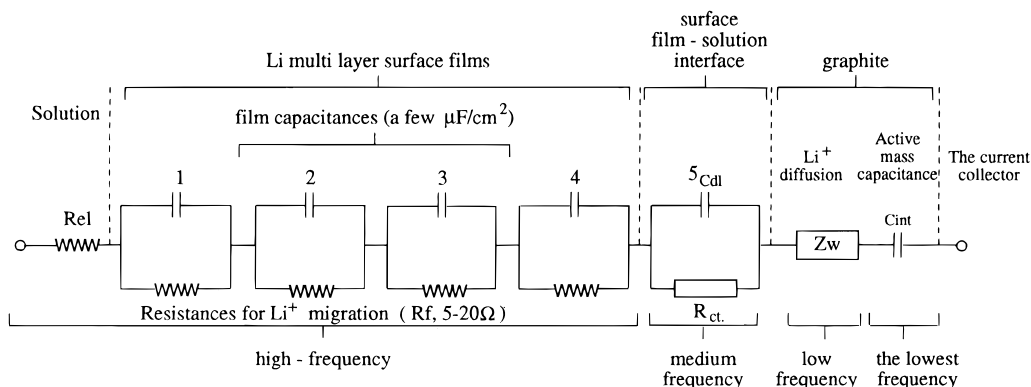
Figure 8. Equivalent circuit analog, which seems to well-present the lithium−graphite intercalation, based on a combination of a Voigt-type analog and the generalized Frumkin and Melik-Gaykazyan impedance. A sketch of the interfacial boundaries of the electrode is also shown.

corresponding to the particle size. The circuit containing the Warburg element is in series with C_{int} (Figure 8).

As already discovered and discussed,[7−9,16] when graphite electrodes are polarized to low potentials in solutions such as the present DMC−EC−LiAsF$_6$ electrolyte system, reduction of the solvents and the salt anion below 1.5V *vs* Li/Li$^+$ precipitates surface films which cover the graphite particles. Hence, intercalation of Li$^+$ into the graphite includes migration through these films. It was found that the surface chemistry thus developed on the graphite particles is very similar to that of Li electrodes in the same solutions. There is spectral evidence (XPS[28]) that these films have a multilayer structure due to difference in their composition as a function of the distance of the surface species precipitated (in a gradual reduction process) from the active reductive electrode surface (Li or Li−C). Impedance spectra measured from Li electrodes and presented as a Nyquist plot have mostly a flat, semicircular shape, which reflects most of the frequency range (100 kHz → a few hertz) measured. As already discussed in detail, these spectra reflect migration of Li ions through surface films of a multilayer structure, which can be modeled quite precisely with a "Voigt"-type equivalent analog of several $R||C$ circuits in series. In this model, each of these $R||C$ circuits relate to Li$^+$ migration through one of the layers comprising the surface films (which has its specific characteristic resistivity and capacitance).

As shown in Figures 4 and 7, all of the Nyquist plots obtained from graphite electrodes contain a flat semicircle belonging to the high-to-medium frequencies, which very much resemble the EIS spectra measured from Li electrodes in the same solutions.[19−21] Consequently, the equivalent circuit analog chosen in this work as the model for the lithium−graphite intercalation electrode (which is based on the FMG model) also includes a Voigt-type analog of about five $R||C$ circuits, which represents Li migration in the surface films and the surface film−solution interface, as already suggested for Li electrodes.[19−21] The completed equivalent circuit analog, which is a modified combination of the FMG and the Voigt-type analogs, is presented in Figure 8. Figure 9 shows a *typical* fit of this equivalent analog with experimental data for the high-to-medium frequencies (ultrathin electrode, 0.075 V, Li/Li$^+$).

A specific feature of this general model is that the solid state diffusion, finite-length diffusion Warburg element is placed in series with C_{dl}. This is due to what is called *unsupported* conditions[25c] for the process under consideration (which means that the same species carry the current by migration and charge transfer). The parallel combination of C_{dl} and Z_w appearing in models of simple electrochemical reactions is valid only for what is called *supported* conditions[25d] (an excess of supporting electrolyte). On the other hand, strict theoretical consideration
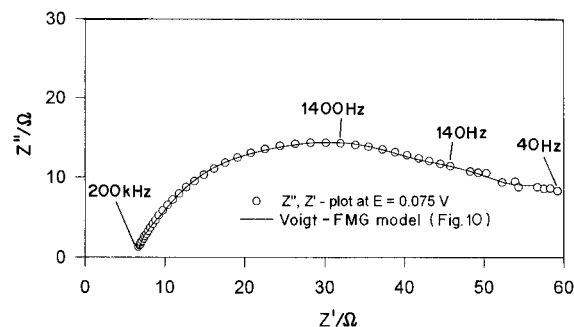
Figure 9. Comparison between a typical experimental Nyquist plot and that calculated using the model of Figure 8 for the high-frequency domain.
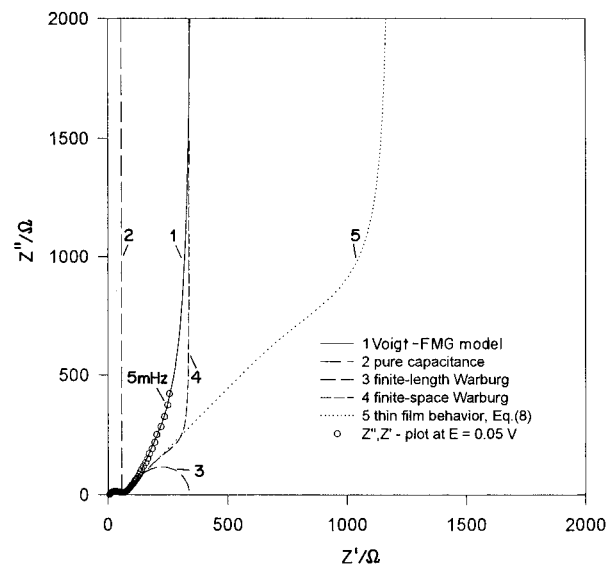
Figure 10. Typical fitting of an experimental Nyquist plot obtained with the ultrathin electrode with different models.

of the impedance response for the unsupported case leads to an equivalent analog containing a *parallel* combination of C_{dl} and an adsorption capacitance C_{ads} *in series* with Z_w.[25e] The choice of the model in Figure 8, in which C_{int} and C_{dl} are in series, is also supported by the results of the theoretical analysis of the complex plane impedance of *thin electroactive polymer film electrodes*.[29]

Figure 10 compares a typical experimental Nyquist plot (measured with an ultrathin electrode at 0.05 V, Li/Li$^+$) with the curve calculated according to the combined Voigt−FMG (denoted as curve 1 in Figure 10). It should be noted that an excellent fit was obtained between experimental data and plots calculated according to this model (both in Nyquist and Bode

EIS and CV of Graphite Electrodes Doped with Li

J. Phys. Chem. B, Vol. 101, No. 23, 1997 **4637**

TABLE 1:   Typical Parameters Obtained by Fitting the Model of Figure 10 to Experimental Data for the Ultrathin Electrode at $E = 0.05$ V *vs* Li/Li^{+a}

Low-Frequency Domain

element	τ/s	R_D/Ω	C_{int}/F
Z_W	75	280	
Z_{fs}	85		0.1
C_{int}			0.1

High-Frequency Domain (Voigt-Type Element)

element	R/Ω	C/μF
first $R\|\|C$ (highest frequencies)	3.2	1.44
second $R\|\|C$	13.8	2.4
third $R\|\|C$	17.7	7.7
fourth $R\|\|C$	12.0	66.6
fifth $R\|\|C$ (medium to low frequencies)	13.5	496

a The accuracy of the data is estimated as ±5%.

TABLE 2:   Potential Dependence of the Low-Frequency Intercalation Capacitance C_{int} Calculated from the EIS Data and from the Slow Scan Rate CV Near Peak e (Phase II → Phase I Transition)^a

	C_{int}/F	
E/V	EIS	CV
0.050	0.098	0.11
0.070	0.23	0.34
0.075 (peak potential)	0.45	1.40
0.080	0.67	0.74
0.085	0.57	0.53
0.090	0.26	0.26
0.095	0.16	0.15

a The error in the measurements and the calculations is estimated at ±5%.

plots). Typical parameters evaluated from the fitting procedure for an ultrathin electrode at a fully intercalated state (0.050 V *vs* Li/Li$^+$) are shown in Table 1. Table 2 presents a comparison between C_{int} as a function of E calculated from the cyclic voltammograms of the low scan rate and $C_{int}(E)$ calculated by fitting experimental EIS data with the modified FMG analog (Figure 10) for the same electrode and conditions (as those for Table 1). As demonstrated in this table, very good agreement was obtained for all of the pairs of values (except for the peak potential) calculated from these two techniques (and the related theoretical treatment). In addition, Figure 10 also presents separate plots of the various elements appearing in the model. Curve 2, which is a vertical line, represents the bulk intercalation capacitance C_{int}. Curve 3 relates to the classical finite-length Warburg-type element Z_w (eq 6)^{25f}

$$Z_w = R_D(j\omega l^2/D)^{-1/2} \tanh(j\omega l^2/D) \quad (6)$$

where R_D is the low-frequency limit of Z_w. For comparison, we have also calculated the plot corresponding to the *finite-space diffusion Warburg*, impedance Z_{fs}^{25,30} (curve 4, Figure 10):

$$Z_{fs} = (\tau/C_{int})(j\omega l^2/D)^{-1/2} \coth(j\omega l^2/D) \quad (7)$$

with the characteristic (solid state) diffusion time $\tau = l^2/D$. The parameters R_D and C_{int} required for calculating curves 3 and 4 are the values calculated by the fitting procedure of the FMG modified model to the experimental data (curve 1 in Figure 10) and have been found to be the optimal ones. Curve 5 in Figure 10 will be discussed later.
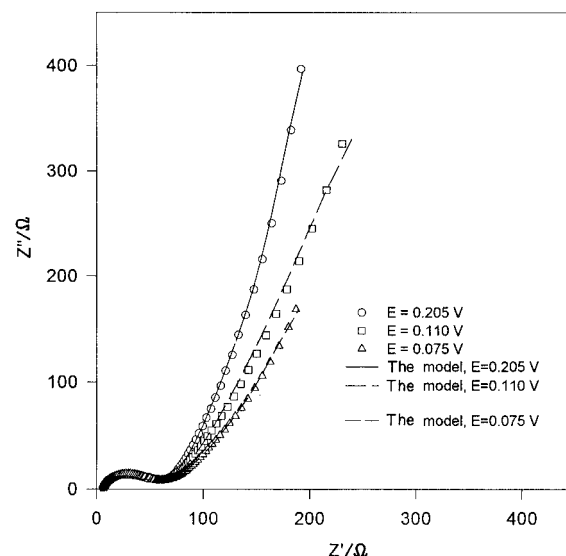

Figure 11. Experimental Nyquist plots for the ultrathin electrode measured around the peak potentials fitted with the model of Figure 8.

Figure 11 further demonstrates the excellent fit obtained between the experimental data and the model in Figure 8.

Discussion

a. High-Frequency Domain. As mentioned above, the high-frequency domain of the impedance spectra measured from ultrathin electrodes (Figure 9) closely resembles that of a Li electrode with similar RC parameters characterizing mainly the migration of lithium ions through the multilayered surface films.$^{17-19}$ There are, however, pronounced differences in the parameters (R_i, C_i) and different types of evolution of the high-frequency spectra with time among ultrathin, thin, and thick electrodes. For the ultrathin electrode (Figure 9), the parameters calculated for the high-frequency domain (R_iC_i of the Voigt-type analog, Table 1) remain constant during intercalation−deintercalation cycles. In contrast, for the thin and the thick electrodes, a considerable increase in the diameter of the semicircle (thin < thick, Figure 4a,b) is observed. These three coatings are different in compression, and thus it is possible that the above differences may reflect different electronic resistance at the graphite particle boundaries on the three electrodes due to the formation of the surface films and their secondary processes with solution species.$^{17-19}$ The contact area between the platelets increases with compression, and thus this resistance should decrease correspondingly (in the order $R_{ultrathin} < R_{thin} < R_{thick}$).

b. Medium- to Low-Frequency Domain. Complex plane impedance plots in Figures 10 and 11 show that at the boundary between the medium- and the low-frequency domains, a unity-slope line appears, which can be modeled by an infinite-length diffusion Warburg $Z_{w\infty}$ element. It is seen from Figure 10 (and can be easily proved analytically) that such an element for the high-frequency limit (without the contribution of the slow interfacial process related to Li migration through the surface films) *is common* to the FMG model and both the finite-length, Z_w, and finite-space diffusion Warburg, Z_{fs}, eqs 6 and 7, respectively.

Figure 10 also shows that at $\omega \to 0$, the FMG impedance and the Z_{fs} element *both* approach one and the same limit connected with the low-frequency intercalation capacity (Figure 10, curves 1 and 4, respectively). Thus, an important feature of the experimental Nyquist plots obtained (as well as of their theoretical simulated FMG curves) is their deviation from the

finite-space diffusion behavior in the medium- to low-frequency domain, which is normally expected for electrodes coated with thin films of redox polymers.[27−37]

c. Comparison with Other Alternative Models. *A priori*, a Warburg-type element that may be a reasonable model for the low-frequency behavior of the spectra measured from lithiated graphite electrodes is the Z_{fs} (finite space, eq 7, Figure 10, curve 4). However, fitting Z_{fs} with experimental parameters (C_{int} and the diffusion time constant τ, eq 7) to actual spectra provided poor fitting at a large domain of low frequencies, as demonstrated in Figure 10. Electrodes comprising coatings of electroactive redox polymers may also prove of interest for the graphite−lithium intercalation. For instance, in the case of Pt/Nafion/Ru(bpy)$_3$$^{2+}$ electrodes,[38] the low-frequency behavior of the impedance spectra measured from them has a trend similar to those spectra measured in the present study. The impedance spectra measured from the Pt/Nafion/Ru(bpy)$_3$$^{2+}$ electrodes could be modeled by two finite space Warburg elements in parallel. This was attributed to the possibility of two separate and independent diffusion paths for ions in the coating which produced two different time constants (one characteristic diffusion length, the coating's thickness δ). This case, however, should be quite different from the present lithium−graphite intercalation, where only *one* diffusion mechanism is expected. This expectation is based on the fact that within a single graphite particle only one diffusion mechanism should take place, and in the active mass as a whole these particles are highly oriented, as discussed above. Indeed, the impedance spectral analysis performed in this work seems to indicate (by the parameter fittings) only one time constant related to solid state diffusion.

Another possible model for the lithiated graphite electrodes may be a homogeneous electroactive polymer film having two transport characteristics of the electronic and the ionic species.[29] The final equation for the impedance of such an electrode in the medium to low frequencies is of the form

$$Z = (\tau/C_{int})(1/[j\omega\tau]^{1/2})[\coth([j\omega\tau]^{1/2}) + $$
$$(t_{e^-} - t_i)^2 \tanh([j\omega\tau]^{1/2})] \quad (8)$$

where t_{e^-} and t_i are the transference numbers for the electronic and ionic species, respectively. Two cases are of particular interest. When both species have the same diffusion coefficient ($t_{e^-} = t_i$), the impedance in eq 8 is reduced to the finite-space Warburg Z_{fs},[29,30,33,34] whereas, at either condition $t_{e^-} > t_i$ or $t_{e^-} < t_i$, both finite Warburg elements appear in eq 8. The physical reason for the involvement of the finite-length Warburg in eq 8 is the nonsymmetry of the concentration profiles in the film, since $D_{e^-} \neq D_i$ and thus $t_{e^-} \neq t_i$.

Since graphite is an excellent electronic conductor, whereas Li$^+$ diffusion through it is rather slow;[15] lithiated graphite electrodes also may be treated as a medium in which the transference numbers of the ionic (Li$^+$) and the electron (e$^-$) charge carriers are quite different. As proposed earlier in this paper, we assume some electronic resistance for the composite electrodes due to possible contact problems between the graphite particles packed onto the current collector. Nevertheless, due to the high difference in conductivity between e$^-$ and Li$^+$ for graphite, we assume that $t_{e^-} > t_i$. Consequently, curves based on eq 8 with C_{int} and τ taken from the experimental data ($t_{e^-} - t_i)^2 \rightarrow 1$ were fitted to experimental impedance spectra measured from lithiated graphite electrodes. A typical example is presented in Figure 10, curve 5. Although the basic trend and feature of curve 5 is similar to the low-frequency shape of the experimental spectra, the fitting obtained is rather poor, as also demonstrated in this figure. Hence, from all of the possible

examples reviewed above, only the FMG model, which combines a finite-length Warburg-type element and bulk capacitance in series, could fit successfully as an excellent match to the experimental impedance spectra measured from the lithium−graphite intercalation electrodes. We propose that eq 8 fails to fit the case of the Li−C intercalation process because this equation reflects the existence of only one extensive property of the electrode, which is its thickness. In our case the graphite electrodes possess two extensive properties: the electrode thickness to which C_{int} proportional and the diffusion length l which depends on the particle size.

d. Very Low Frequencies: Dynamics of Phase Transition in Lithiated Graphite. Close examination of Figures 4b, 7a−c, and 10 show that the lowest applied frequency (5 mHz) was not, in fact, sufficiently small to reach the vertical line (purely capacitive behavior). Comparison between the Nyquist plots of the simple intercalation model (Figure 6) and that of the more realistic FMG model (Figure 10) clearly reveals some contribution of the solid state diffusion of lithium ions to the low-frequency capacitive behavior. However, the predominance of the capacitive contribution in the impedance at $\omega/2\pi = 5$ mHz is proven by the characteristic peak-shaped behavior of the Z'' component of the electrode's impedance at various potentials, around the CV peak potential (Figures 6 and 7). The minimum of Z'' certainly corresponds to the maximum in C_{int}. Thus, the entire potential dependence of C_{int} closely resembles the CV peak (Figure 2).

Qualitatively, similar correlations have been observed for a number of electroactive polymer films.[32,36,39]

In order to quantitatively correlate the obtained EIS and CV results, we need to estimate the characteristic time windows of these experiments. Substituting the experimental values $\nu = 4$ μV/s and $\omega/2\pi = 5$ mHz into the formulas $RT/F\nu$ and ω^{-1} for the CV and EIS, respectively, yields the value of ca. 6.4×10^3 s for the CV and 30 s for the EIS. As the time window of these measurements is longer, there is a better possibility of probing the consumption−accumulation step of the intercalation, as well as the thermodynamics of the phase transition, without the interference of diffusion processes. From this point of view, the application of slow scan CV may be highly advantageous for the study of these processes beyond diffusion control.

When (as usual) EIS measurements at too low frequencies are not available, the degree of agreement between the intercalation capacity at ω extrapolated to zero and that calculated from the corresponding slow scan CV may be a good test for estimation of the reliability of the proposed model. This comparison is shown in Table 2, which shows good matching in the intercalation capacity for all potentials except for the peak potential. It seems that the potential dependence of the intercalation capacitance is steeper than that observed by the EIS. Thus, the 5 mV potential difference between the base potentials of the EIS measurements is not sufficiently small to exactly match the peak of the capacity.

Another possible source of error in obtaining reliable CV curves may be ohmic drops of potential. In addition to the uncompensated potential drop in the electrolyte, possible ohmic drops in the surface films covering the graphite particles also need to be considered. (We assume that the surface films−electrode interface does not contribute to the total applied potential). The usual solution resistance measured by EIS is about 10−15 Ω. Multiplying it by a typical peak current of about 1.4×10^{-4} A ($\nu = 4 \mu$V/s) yields an ohmic drop of about 2.1 mV. This is close to the difference in potentials observed between the peak potentials of the CV and the corresponding maxima in the low-frequency capacitance (as reflected by the

EIS and CV of Graphite Electrodes Doped with Li

J. Phys. Chem. B, Vol. 101, No. 23, 1997 **4639**
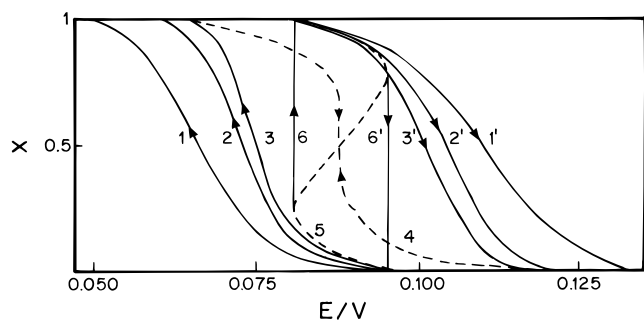
Figure 12. Charging curves obtained for the ultrathin electrode by integration of the charge in the CV plots (Figure 4) at different ν: (1, 1') -15 μV/s; (2, 2') -7 μV/s; (3, 3') -4 μV/s. Curves 4 and 5 represent Frumkin isotherms calculated according to eq 2 with different parameters: (4) $g = -4$ and (5) $g = -6$. Isotherm 6,6' is a modified isotherm (5) (by the tangent lines) and represents the realistic case of high attractive interactions among the intercalation sites (a phase transition within a very narrow potential window).

minima in Z'' at the lowest frequency). Hence, we conclude that the ohmic drop in the worst case can probably somewhat distort the very narrow CV peaks, but is not an important factor, as the peak-potential separations are of tens of millivolts.

From the above discussion (results, section c and Figures 2, 3, and 5) it is clear that the process reflected by the cyclic voltammograms depends strongly on the thickness of the coating. Very narrow (about 10 mV half-peak width) slow scan rate CV of the highly oriented ultrathin electrodes could not be quantitatively described by eq 1, and thus, we assume that they mostly reflect the dynamics of the accumulation of Li into graphite and the phase transition between the different lithium–graphite stages. In contrast, slow scan CV of the thicker electrodes also reflects some charge transfer complications which related to their less oriented structure. Their source may be ionic migration through the more complicated SEI, possible electronic resistance across the boundaries of the particles, and some minor continuous reduction of solution species (because of defects in the passivating surface films).

The voltammetric curve obtained with the ultrathin electrodes is very similar to those theoretically predicted for the doping processes of electroactive polymers with strong, short-range particle interaction.[40] However, consideration of the short-range, instead of long-range, interactions requires only slight modification of the Frumkin isotherm (eq 2).[40] The common property of the isotherms of this type is that at $g < g_{critical}$ ($g_{critical} = -4$); it is practically impossible to inject *continuously* the charge keeping the single host matrix phase. Consequently, at some degree of intercalation (or doping) a phase transition through a "droplets" formation mechanism[40–42] takes place. This mechanism is, in fact, similar to the description of staging phenomena during the intercalation of lithium into graphitic carbons.[43,44] The dynamics of the phase transition between the various lithium–graphite compounds, which is reflected in the purest manner by the slow scan CV of the ultrathin electrodes, can be better illustrated using charging curves which are, in fact, intercalation isotherms for equilibrium conditions following the approach advanced in ref 40. Three curves from 1 to 3 in Figure 12 were obtained by integration of the voltammetric peak e and its corresponding anodic peak (see Figure 2) for three different scan rates (Figure 3). Considerable hysteresis, which increases with ν, characterizes these curves. Curve 4 was calculated according to the Frumkin isotherm (eq 2), with $g_{critical} = -4$, whereas when $g < g_{critical}$, an S-shaped isotherm is obtained. Curve 5 relates to an isotherm with $g = -6$. Note that the center of symmetry of the theoretical isotherms matched well with the experimental mid-peak potential.

The vertical line at the middle of curve 4 in Figure 12, which refers to the equilibrium phase transition (in both directions), cannot be reached practically, since there is an intrinsic hysterisis between the forward and backward phase transitions due to an energy barrier.

Assuming that the model of adsorption type behavior with strong attraction forces is basically valid for describing the voltammetry of the lithium–graphite intercalation process, the relevant intercalation isotherms for these processes, according to eq 2, should indeed include a highly negative g value which may be even lower than $g_{critical}$. In this case, the theoretical isotherm is s-shaped, like that of curve 5 in Figure 12. However, such an isotherm cannot be realistic. As the potential is shifted toward the negative values, with a resultant increase of X, at the first point of deflection (low X, curve 5)—i.e., the theoretical ability to intercalate more Li at higher potentials due to the attraction forces—a transition from a low- to high-lithium containing phase occurs drastically at a practically constant potential. Hence, an intercalation isotherm as presented by curve 6 should be obtained (theoretically). This potential is, of course, more negative than is the standard one, E_0'. Deintercalation proceeds according to a similar, reverse scenario, thus resulting in reverse phase transition at $E > E_0'$. The distance between the vertical lines of curve 6, in fact, marks the *intrinsic hysteresis* in the X vs $(E - E_0')$ curves, which is indeed close to the experimental peak-potential separation, ca. 30 mV. Hence, an isotherm such as curve 6 in Figure 12 reflects the dynamic of the phase transition close to thermodynamic control.

The deviation of the experimental isotherms 1–3 from the vertical lines of curve 6 may be generally connected with various relaxation processes like diffusion, slow charge transfer, etc. We have shown above, however, that, for the ultrathin electrode, the major process responsible for the behavior of the ultrathin electrodes at slow scan CV, and which explains the shape of the CV peaks, is the formation of clusters of the phase with higher lithium content (with a relatively small involvement of the other processes). The increase in ν results in broadening of the CV peak, and thus the isotherm becomes more flat, like curves 3 to 1 in Figure 12. Further increase in ν (at $\nu > \nu_{critical}$ completely changes the CV behavior from being controlled by accumulation–consumption to being solid state diffusion controlled.[12] It is clear from the present study that the thicker the coating, the smaller the critical scan rate $\nu_{critical}$, above which the behavior becomes diffusion controlled.

Conclusion

Li intercalation into graphite involves several processes which occur in series: diffusion of Li ions in solutions, charge transfer, migration of Li ions through the surface films which cover the graphite particles, solid state diffusion of Li ions into the graphite, and, finally, accumulation–consumption of Li in graphite, which accompanies phase transition between intercalation stages. When thin electrodes are used, in which the graphite platelets are highly oriented and ordered, all of these processes are nicely reflected by impedance spectroscopy and are well-separated, going from high to low frequencies, respectively, in the Nyquist or Bode plots obtained. A very logical model for these processes is an equivalent circuit analog combining a Voigt-type analog (several $R||C$ circuits in series), which represents the migration of lithium through the surface films and the charge transfer in the film–solution interface, in series with a Warburg–type element representing solid state diffusion of lithium in the graphite and a capacitance representing the charge accumulation by the intercalating species. An excellent

fit was indeed obtained between the spectra calculated on the basis of this model and the experimental EIS data obtained. The cyclic voltammograms obtained from thin graphite electrodes (micronic thickness) could be nicely fitted by a model based on an adsorption process with high-attraction interactions among intercalation sites, accompanied by a slow charge transfer whose thermodynamics may be described by a modified Frumkin-type isotherm.

The basic scenario of the entire intercalation of Li into graphite may be summarized as follows. A first polarization of graphite in Li salt solutions to low potentials leads to formation of surface films which precipitate on the graphite particles and form a stable protective envelope in the case of EC−DMC LiAsF$_6$ solutions. At a steady state, the intercalation involves Li$^+$ migration through these surface films followed by solid state diffusion of Li ions into the graphite. Simultaneously, electron transfer across the boundaries of the graphite particles, partly covered with the surface films, takes place and balances the flux of the Li$^+$ ions. Both fluxes form intercalation stages in which high-attraction interactions exist among intercalation sites. When the stage is fully developed, the new phase, which is richer in lithium, is formed, probably in droplets within the bulk of the previous stage.

This work also demonstrates the influence of the electrode's morphology on the resolution of the processes' analysis by parallel EIS and CV measurements.

References and Notes

(1) Dahn, J. R.; Fong, R.; Spoon, M. *J. Phys. Rev. B.* **1990**, *42*, 6424.

(2) Dahn, J. R.; Sligh, A. K.; Shi, H.; Way, B. W.; Weydanz, W. J.; Reimers, J. N.; Zhong, Q.; von Sacken, U. In *Lithium Batteries-New Materials, Developments and Perspectives*; Pistoia, G., Ed.; Elsevier: Amsterdam, 1994; p 1.

(3) Ohzuku, T.; Iwakoshi, Y.; Sawai, K. *J. Electrochem. Soc.* **1993**, *140*, 2490.

(4) Megahed, S.; Scrosati, B. *J. Power Sources* **1994**, *51*, 79.

(5) Peled, E. In *Rechargeable lithium and lithium-ion batteries*; Megahed, S., Barnett, B. M., Like, X. Eds.; Battery Division, Proceedings Vol. 94−28; The Electrochemical Society: Pennington, NJ, 1995; p 1.

(6) Zaghib, K.; Tatsumi, K.; Abe, H.; Ohsaki, T.; Sawada, Y.; Higuchi, S. In *Rechargeable lithium and lithium ion batteries*; Megahed, S.; Barnett, B. M., Like, X., Eds.; Battery Du Proceedings Vol. 94-28; the Electrochemical Society: Pennington, NJ, 1995; p 121.

(7) Yazami, R.; Deschamps, M. In *Rechargeable lithium and lithium ion batteries*; Megahed, S.; Barnett, B. M., Like, X., Eds.; Battery Du Proceedings Vol. 94-28; the Electrochemical Society: Pennington, NJ, 1995; p 183.

(8) Aurbach, D.; Ein-Eli, Y.; Chusid, O.; Babai, M.; Carmeli, T.; Yamin, H. *J. Electrochem. Soc.* **1994**, *141*, 603.

(9) Aurbach, D.; Ein-Eli, Y.; Markovsky, B.; Carmeli, Y.; Yamin, H.; Luski, S. *Electrochim. Acta* **1994**, *39*, 2559.

(10) Guyomard, D.; Tarascon, J. M. *J. Electrochem. Soc.* **1992**, *139*, 937.

(11) Takami, N.; Satoh, A.; Hara, M.; Ohsaki, T. *J. Electrochem. Soc.* **1995**, *142*, 371.

(12) Morita, M.; Nishimura, N.; Matsuda, Y. *Electrochim. Acta* **1993**, *38*, 1721.

(13) Uchida, T.; Morikawa, Y.; Ikuta, H.; Wakihara, M. *J. Electrochem. Soc.* **1996**, *143*, 2606.

(14) Levi, M. D.; Aurbach, D. *J. Electroanal. Chem.* **1997**, *421*, 79.

(15) Levi, M. D.; Levi, E. A.; Aurbach, D. *J. Electroanal. Chem.* **1997**, *421*, 89.

(16) Aurbach, D.; Levi, M. D.; Levi, E. A.; Schechter, A. *J. Phys. Chem. B* **1997**, *101*, 2195.

(17) Aurbach, D. *J. Electrochem. Soc.* **1989**, *136*, 906, 1606, 1611.

(18) Aurbach, D.; Gottlieb, H. E. *Electrochim. Acta* **1989**, *34*, 141.

(19) Aurbach, D.; Zaban, A. *J. Electroanal. Chem.* **1993**, *348*, 155.

(20) Aurbach, D.; Zaban, Z. *J. Electroanal. Chem.* **1994**, *367*, 15.

(21) Aurbach, D.; Zaban, A. *J. Electroanal. Chem.* **1994**, *365*, 41.

(22) Bockris, J. O.'M.; Khan, S.U.H. *Surface Electrochemistry, A Molecular Level Approach*, Plenum Press: New York, London, 1993; Chapter 3, p 224.

(23) Angerstein-Kozlowska, H.; Kleinger, J.; Conway, B. E. *J. Electroanal. Chem.* **1977**, *75*, 45.

(24) Bard, A.; Faulkner, L. *Electrochemical Methods. Fundamentals and Applications*; Wiley: New York, 1980; p 101.

(25) MacDonald, J. R. *Impedance Spectroscopy. Emphasizing Solid Materials and Systems*; Wiley: New York, 1987; (a) p 75, (b) p 103, (c) p 107, (d) p 101, (e) p 114, (f) p 60.

(26) Stoynov, Z.; Grafov, B.; Savova-Stoynova, B.; Elkin, V. *Electrical Impedance* (in Russian); Nauka: Moscow, 1991; (a) p 27, (b) p 67.

(27) Frumkin, A. N.; Melik-Gaykazyan, V. I. *USSR Acad. Sci. Rep.* **1951**, *77*, 855.

(28) Aurbach, D.; Weissman, I.; Schechter, A.; Cohen, H. *Langmuir* **1996**, *12*, 3991.

(29) Vorotyntsev, M. A.; Daikhin, L. I.; Levi, M. D. *J. Electroanal. Chem.* **1994**, *364*, 37.

(30) Buck, R. P. *J. Electroanal. Chem.* **1986**, *210*, 1; **1987**, *219*, 23.

(31) Inzelt, G., Bard, A. J., Eds. *Electroanalytical Chemistry*; Dekker: New York, 1994; Vol. 18, p 89.

(32) Ren, X.; Pickup, P. *J. Phys. Chem.* **1993**, *97*, 5356.

(33) Ho, C.; Raistrick, D.; Huggins, R. A. *J. Electrochem. Soc.* **1980**, *127*, 343.

(34) Franceschetti, D. R.; MacDonald, J. R. *J. Electrochem. Soc.* **1982**, *129*, 1754.

(35) Mathias, M. F.; Haas, O. *J. Phys. Chem.* **1992**, *96*, 3174.

(36) Glarum, S. H.; Marshall, J. H. *J. Electrochem. Soc.* **1980**, *127*, 1467.

(37) Deslouis, C.; Musiani, M. M.; Pagura, C.; Tribollet, B. *J. Electrochem. Soc.* **1991**, *138*, 2606.

(38) Rubinstein, I.; Rishpon, J.; Gottesfeld, S. *J. Electrochem. Soc.* **1986**, *133*, 729.

(39) Vieil, E. *J. Electroanal. Chem.* **1991**, *297*, 61.

(40) Vorotyntsev, M. A.; Badiali, J. P. *Electrochim. Acta* **1994**, *39*, 289.

(41) Abraham, F. F. *Homogeneous Nucleation Theory*; Academic Press: New York, 1974.

(42) Gunton, J. D.; San Miguel, M.; Sahni, P. S. *Phase Transitions* **1983**, *8*, 267.

(43) Daumas, N.; Herold, A. *C.R. Seances Acad. Sci. Ser. C* **1969**, *286*, 373.

(44) Safran, S. A. *Phys. Rev. Lett.* **1980**, *44*, 937.